

Low-temperature single crystal reflection spectra of forsterite

H. Suto,^{1*} H. Sogawa,² S. Tachibana,³ C. Koike,² H. Karoji,¹ A. Tsuchiyama,⁴
H. Chihara,⁴ K. Mizutani,⁵ J. Akedo,⁶ K. Ogiso,⁶ T. Fukui⁷ and S. Ohara⁸

¹National Astronomical Observatory Japan, Mitaka, Tokyo, Japan

²Kyoto Pharmaceutical University, Yamashina, Kyoto, Japan

³University of Tokyo, Department of Earth and Space Science, Hongo, Tokyo, Japan

⁴Osaka University, Department of Earth and Space Science, Toyonaka, Osaka, Japan

⁵National Institute of Information and Communication Technology, Koganei, Tokyo, Japan

⁶National Institute of Advanced Industrial Science and Technology, Tsukuba, Ibaragi, Japan

⁷Hosokawa Powder Technology Research Institute, Hirakata, Osaka, Japan

⁸Institute of Multidisciplinary Research for Advanced Materials, Tohoku University, Sendai, Miyagi, Japan

Accepted 2006 May 17. Received 2006 May 10; in original form 2006 February 10

ABSTRACT

The infrared reflectivities of crystalline forsterite (Mg_2SiO_4) were measured for the temperature range 295–50 K for each crystal axis, between wavenumber 5000 and 100 cm^{-1} . The reflection spectra show clear dependence of temperature; most of the bands become more intense, sharper and their peak positions shift to higher wavenumber with decreasing temperature. Reflection spectra were fitted with dispersion formula of damped oscillator model of the dielectric constants and the oscillator parameters in the model were derived. The absorption spectra of forsterite particle are calculated with the derived dielectric constants to show that the forsterite features are good thermal indicator for cold temperature range below 295 K.

Key words: methods: laboratory – circumstellar matter – dust, extinction – ISM: lines and bands.

1 INTRODUCTION

Silicate dust is one of the major components of interplanetary and interstellar solid particles, and the crystalline form of silicate such as forsterite and enstatite is now believed to exist in comets, and the dense circumstellar regions around some of evolved and pre-main-sequence stars based on the spectral identifications by *ISO*, and ground-based telescope infrared observations (Waelkens et al. 1996; Waters et al. 1996, 1998; Malfait et al. 1998; Molster et al. 1999; Honda et al. 2003).

Observed 69- μm feature is identified with one of forsterite features (Malfait et al. 1998), and Bowey et al. (2002) and Molster et al. (2002) noted that the blueward shift and narrowing of 69- μm emission band of forsterite make promising diagnostics of characteristic temperature of crystalline dust. Laboratory works were conducted to investigate the temperature dependence of crystalline silicates and the absorption spectra of silicate particles were measured in low temperatures (Bowey et al. 2001, 2002; Chihara, Koike & Tsuchiyama 2001; Koike et al. 2006). The absorption peak at 69 μm measured in laboratories shifted towards shorter wavelength with decreasing temperature, and the comparison of the laboratory data with *ISO* data suggested that the astronomically observed crystals have temperature about 150 K or below. The observed features

around 20–40 μm also suggested low temperature around 100 K or below (Molster et al. 2002). Laboratory studies play a fundamental role in analysing the observational results, and reliable optical characters of crystalline silicates in low temperature are desired for interpretation of observed features, and modelling the circumstellar dust disc.

Absorption measurement of powder samples in laboratory is a conventional way to look into the thermal behaviour of the infrared features of solids, but the absorption spectra by powder depend on the shape distribution, the size distribution and the coagulation degree of samples, which are difficult to be regulated. Because of those uncontrolled factors, the particle absorption spectra obtained in laboratory are not identical between the prepared samples even though they contain the same species. It is also difficult to know which optical axis an absorption feature belongs to. On the other hand, if we are able to obtain a single crystalline sample with good quality and reasonable size, its reflection measurements at infrared region provide with little ambiguity the dielectric or optical constants of crystal's each optical axis, which is vital for accounting the radiation characters of crystalline dust.

Crystalline forsterite (Mg_2SiO_4) belongs to olivine series whose point group is D_{2h}^{16} . The lattice vibrations have been investigated by some authors (Servoin & Piriou 1973; Iishi 1978; Hofmeister 1987; Reynard 1991; Fabian, Henning & Jager 2001). Sogawa et al. (2006) recently revised the oscillator parameters at room temperature over wavelength up to 100 cm^{-1} . But no oscillator parameters or no

*E-mail: suto@naoj.org

optical constant has been obtained for temperature below 295 K as far as we know. We measured the reflection spectra of single crystalline forsterite (Mg_2SiO_4) in infrared region ($5000\text{--}100\text{ cm}^{-1}$, or $5\text{--}100\text{ }\mu\text{m}$) at room and low temperatures (from 295 to 50 K), and derived the oscillator parameters by fitting reflection spectra with dispersion formula of damped oscillator model. Our parameters provide a unique set of dielectric constants of crystalline forsterite for temperature down to 50 K in the infrared region and are useful for identifying cosmic forsterite, estimating the temperature of cosmic silicate crystal and establishing the model of the dusts in the Solar system as well as circumstellar dust around the evolved and young stars.

2 EXPERIMENTAL METHODS

To make a cryogenic condition, we prepared a vacuum chamber located below the cryo cooler head. The chamber contains a small compartment which embraces a cold stage, where a forsterite sample and a calibration mirror were held down with copper plates to ensure good thermal contact between the sample and the cold stage. The cold stage is able to be slid horizontally by pulling or pushing the coupling rod inserted from the outside through the chamber wall. Flexible copper meshes were used as the thermal conductor between the cold stage and the end of the cold head. An ohmic heater and a silicon diode temperature sensor were on the stage and the sample temperature was controlled within accuracy of a few degree by a Lakeshore temperature controller. The cold head was supported above the spectrometer using the stage which is adjustable in three-dimensional parallel shift, rotation and tilt about vertical axis so that the sample position and direction were aligned appropriate to the infrared beam for each reflection measurement. 2-mm thick KRS5 and polyethylene discs were used for the window on the chamber. They were set tilted to divert the reflection by the window surfaces away from the path to the detector. The cold stage in the chamber has the square holes below the sample and the calibration mirror for receiving the beam from the spectrometer.

Forsterite single crystal was grown by the Czochralski method (Takei 1978). The purity of the crystal is more than 99 per cent.

Three pieces of centimetre size crystal were prepared from a large single crystal, and crystalline axes were determined by X-ray precession method. The three pieces were polished to make the (100), (010) and (001) surfaces. Reflections whose electric field polarized parallel to the axis a were measured on (100) surface, axis b on both (100) and (001), axis c on both (100) and (010). The data were reduced to the final spectrum selecting those with the higher reflectivities among the measurements and eliminating those with anomalous features. Reflection spectra were taken with Nicolet Fourier spectrometer in the range of $5000\text{--}100\text{ cm}^{-1}$ with wire grid polarizer of KRS5 substrate ($5000\text{--}230\text{ cm}^{-1}$) and polyethylene substrate ($230\text{--}100\text{ cm}^{-1}$). A KBr and a solid substrate beamsplitter were used for the range $5000\text{--}400$ and $600\text{--}100\text{ cm}^{-1}$, respectively, coupled with DTGS detectors with KBr and polyethylene windows. Spectral resolution was 1 cm^{-1} as well as 0.5 and 0.25 cm^{-1} in case that we need to resolve narrow features and the steep edges of wide features. A customized optical module was employed to fold the spectrometer beam to and from the sample compartment through the window at the bottom of the vacuum chamber. The incident angle of the beam to the normal direction of sample surface is 10° . The reflectance of the sample was calibrated using a gold-coated mirror that was placed next to a sample and slid into the beam path on the same position with the forsterite sample before and after the sample measurements. The absolute reflectance of the gold mirror was measured at visible and infrared up to $2.5\text{ }\mu\text{m}$ whose reflectance was constant, 99 per cent from 1.5 to $2.5\text{ }\mu\text{m}$. 99 per cent of reflectance for all wavelength was assumed for the gold mirror.

3 RESULTS

3.1 Reflection spectra

There were rich features observed in the reflection spectra for each crystalline axis of forsterite. The measured spectra were shown in Fig. 1. Olivine crystal belongs to the space group D_{2h}^{16} , and there are 35 (nine B_{1u} , 13 B_{2u} and 13 B_{3u}) or 38 (10 B_{1u} , 14 B_{2u} and 14 B_{3u}) infrared active optical modes expected from symmetry analysis (Iishi 1978; Hofmeister 1987). In our measurements, eight in

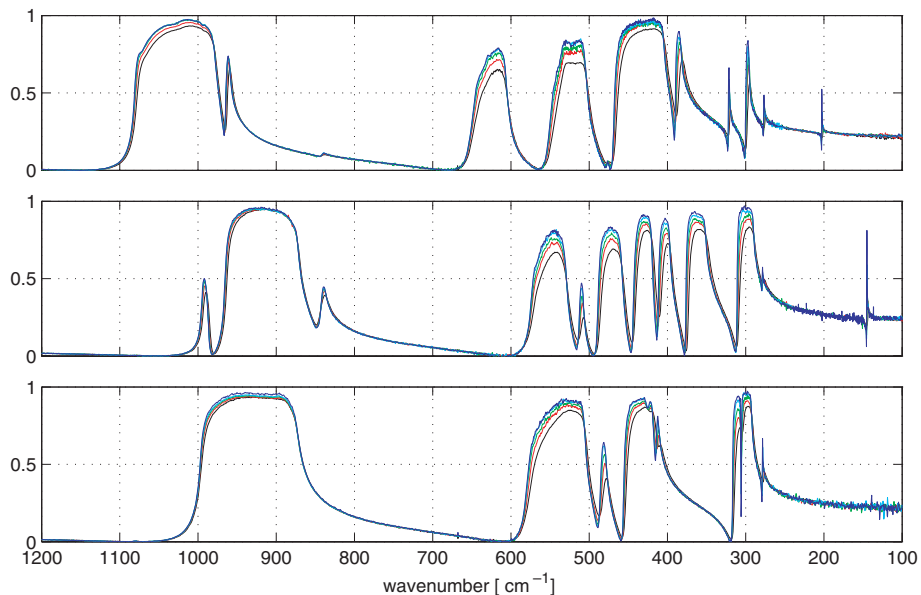


Figure 1. Reflection spectra of forsterite for the axis a (top panel), b (middle panel) and c (bottom panel) and temperatures 295 K (black), 200 K (red), 150 K (green), 100 K (cyan) and 50 K (blue). The vertical coordinate is reflectivity.

axis c (B_{1u}), 12 in axis b (B_{2u}) and 11 in axis a (B_{3u}) features were clearly observed. The small bumps at 475 cm^{-1} in axis a , and at 420 cm^{-1} at axis c were also observed, but these were neglected in the next section of oscillator analysis because of their smallness and non-proper fit by the oscillator model.

The features were assigned as Si–O stretching and bending ($1000\text{--}500\text{ cm}^{-1}$, $10\text{--}20\text{ }\mu\text{m}$), SiO_4 rotation ($500\text{--}400\text{ cm}^{-1}$, $20\text{--}25\text{ }\mu\text{m}$) and Mg translation ($400\text{--}140\text{ cm}^{-1}$, $25\text{--}70\text{ }\mu\text{m}$) by Iishi (1978). The most intense and broad features at 1000 cm^{-1} in axis a , 900 cm^{-1} in axes b and c showed small change with decreasing temperature. The reflectivity of these bands increases slightly; band positions and their widths exhibit little change with decreasing temperature. The bond angle and length between Si and O in SiO_4 tetrahedra should be stable for the temperature range measured, and these modes are not good thermo indicator for the temperature below 295 K. The small feature at 840 cm^{-1} in axis a shows little change with temperature as well. The features 990 , 840 cm^{-1} in axis b and 960 cm^{-1} in axis a increase their intensities and shift peak position to higher wavenumber, but their thermal developments are weak.

The features at 620 , 550 and 530 cm^{-1} for axes a , b and c , respectively, have shape slanted towards shorter wavenumber, which could be characteristic to the bending mode of Si and O in forsterite. The damped oscillator model in the next section does not reproduce these features accurately.

All features lower than 500 cm^{-1} show systematic change, more intense, sharper and shift to higher wavenumber with decreasing temperature, that is interpreted as bonding force between atoms increases and non-harmonic phonon–phonon interaction decreases as temperature reduced. The intriguing change is the splitting of two features 310 and 300 cm^{-1} in axis c as temperature reduced, the reflectivity at the bottom of trough between the features decreased drastically from 0.7 to 0.2 (see Fig. 2),

The features at lower wavenumber due to the translation mode of Mg atom become sharp remarkably as temperature decreased.

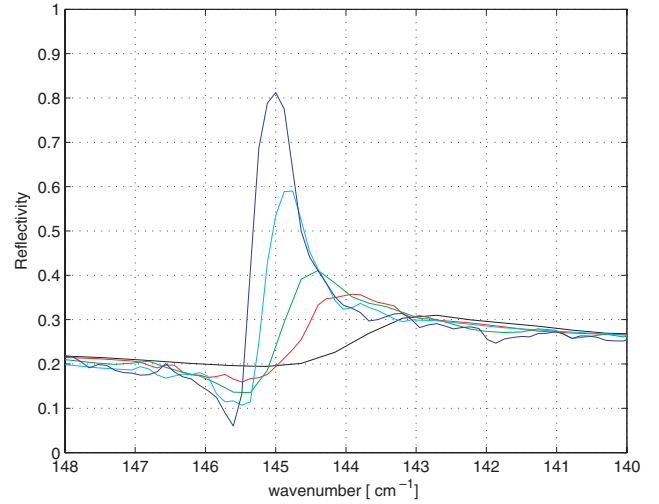


Figure 3. Reflection feature of forsterite for the axis b at 140 cm^{-1} ($69\text{ }\mu\text{m}$). Each line is for 295 K (black), 200 K (red), 150 K (green), 100 K (cyan) and 50 K (blue).

Especially the feature at 140 cm^{-1} ($69\text{ }\mu\text{m}$) in axis b shows the outstanding alternation as shown in Fig. 3. The reflectivity above continuum level increased about one order, the width decreased four times and the peak position shifted 1 per cent higher as temperature went down from 295 to 50 K. This band is well isolated from other features, and a promising temperature diagnostic in forsterite crystal. The feature at 200 cm^{-1} in axis a is also well isolated and manifested large change with temperature as in the same order of 140 cm^{-1} feature as shown in Fig. 4. Since this feature is very weak at temperature above 150 K, it will provide a definite proof of existence of cold dust if its prominent absorption or emission feature is observed.

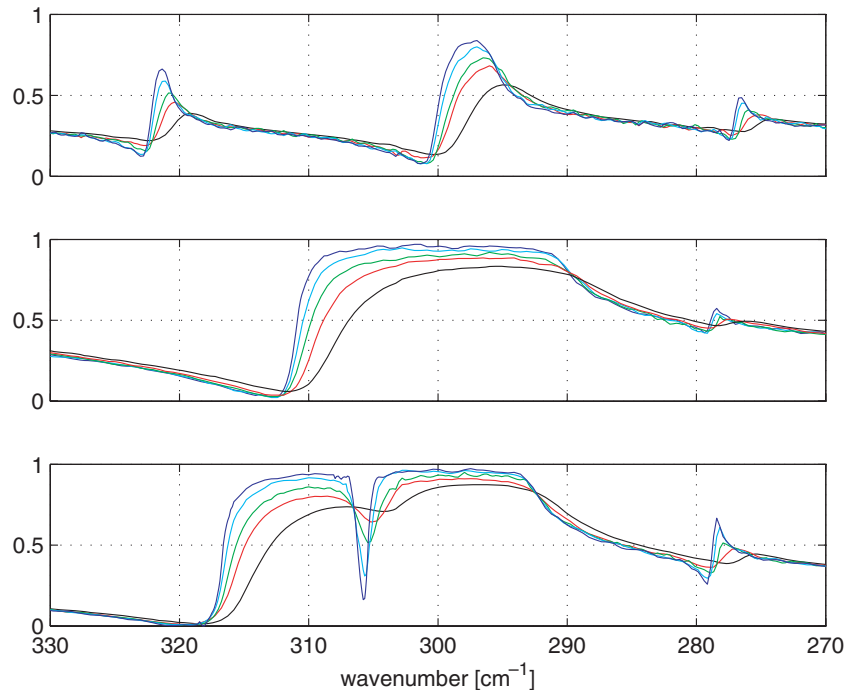


Figure 2. Expanded view of reflection spectra of forsterite at $330\text{--}270\text{ cm}^{-1}$ for the axis a (top panel), b (middle panel) and c (bottom panel) and temperatures 295 K (black), 200 K (red), 150 K (green), 100 K (cyan) and 50 K (blue).

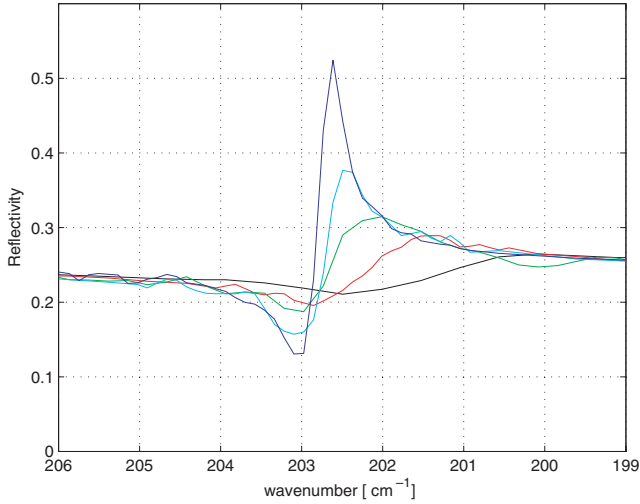


Figure 4. Reflection feature of forsterite for the axis *a* at 200 cm^{−1} (50 μm). Each line is for 295 K (black), 200 K (red), 150 K (green), 100 K (cyan) and 50 K (blue).

The continuum level at region higher than 1200 cm^{−1}, and lower than 200 cm^{−1} did not show significant change with decreasing temperature. The levels of slopes at 800–600 cm^{−1} in axes *b* and *c* show little variation. These suggest that the degree of polarity of dipole moment in the lattice is quite stable to the change of temperature.

3.2 Oscillator parameters for dielectric constant

The dielectric constants were derived from the reflection spectra by adopting the classical dispersion model of damped oscillator. The dispersion relation at wavenumber ω is expressed as

$$\epsilon(\omega) = \epsilon_{\infty} + \sum_j \frac{S_j}{(\omega_j^2 - \omega^2 - i\gamma_j\omega)}, \quad (1)$$

where ϵ_{∞} is the dielectric constant representing the contribution from higher wavenumber, S_j , ω_j and γ_j are the oscillator strength, resonant wavenumber and damping factor, respectively. The reflectivity R is calculated from dielectric constant ϵ as

$$R = \left| \frac{\sqrt{\epsilon - \sin^2(\theta)} - \cos(\theta)}{\sqrt{\epsilon - \sin^2(\theta)} + \cos(\theta)} \right|^2, \quad (2)$$

where θ is the beam incident angle to a sample surface. In our reflectance module, the incident angle is 10°, almost normal to the surface.

The oscillator parameters were searched in minimizing the difference between the measurement and calculation. 11, 12 and eight oscillators were considered for axes *a*, *b* and *c*, respectively. The derived parameter values are listed in Table 1 for each crystalline axis and temperature. The oscillator model with our parameter values reproduces measured spectra fairly well as shown in Fig. 5 as an example, that is the case of axis *b* and temperature 200 K. The shapes, intensities and positions of features and continuum levels are generally well reconstructed.

However, there are portions on the spectra where the fitting is not perfect. For features in axis *a*, a small dip was observed at the 1100 cm^{−1}, top of the strong wide feature of 1000 cm^{−1}. As we assumed the band at 1000 cm^{−1} as single one, this dip is not reproduced by our parameters. The upper part of the feature at 620 cm^{−1}

is slanted towards small wavenumber and a single Lorentz oscillator cannot reproduce this off-symmetry shape well. The top of feature at 520 cm^{−1} is very flat with width about 20 cm^{−1}. The Lorentz model cannot reproduce a feature posing such a flat top. Another small feature is at 470 cm^{−1} but this feature is not included in the fitting because it is too small to fit properly.

For the features in axis *b*, the bands from 500 to 300 cm^{−1} are hard to be fitted precisely for their low trough level and top peak level simultaneously, although the fitting error is less than 5 per cent. The error could be reduced by assuming a wavenumber dependence of the damping factor γ , where γ decrease as wavenumber comes off the resonance wavenumber ω_j . Quantum mechanical calculations considering non-harmonic potential term concluded the dependence of γ on wavenumber, and its dependence is function of density of states (Maradudin & Wallis 1960), but exact explicit formula of wavenumber dependence for γ is not known, and as the difference between the measurements and calculation is not large, we treat the factor γ as constant parameter. The feature at 550 cm^{−1} is slanted towards small wavenumber, and poorly fitted.

For features in axis *c*, the feature at 530 cm^{−1} is also slanted towards small wavenumber which is similar to the feature at 620 cm^{−1} in axis *a*, and 550 cm^{−1} in axis *b*, which cannot be reproduced well with single oscillator. A small dip was observed on the top of feature 420 cm^{−1}. There could be a small oscillator in this spot, but this dip is small, and no split or no temperature dependence was observed, then we assume the feature as of single oscillator.

The resonant wavenumber ω_j increases with decreasing temperature, and the fractional changes of resonant wavenumber $\omega_j(T)/\omega_j(T = 295)$ are generally large for the features at lower wavenumber comparing to those at higher wavenumber. The increase of resonant wavenumber is conspicuous when temperature changes between 295 and 200 K, and becomes less at temperature below 100 K. The total shift is 1 per cent at most from 295 to 50 K. The ratio of the damping factor $\gamma_j(T)/\gamma_j(T = 295)$ decreases with decreasing temperature. The change of damping factor with temperature is also larger for the features at lower wavenumber comparing to those at higher wavenumber, and almost linearly decreases towards lower temperature. Since the γ factor controls the bandwidth of absorption and emission feature, the full width at half-maximum (FWHM) of observed feature can be a sensitive indicator of temperature at lower temperature. The strength factor S_j shows weak temperature dependence, almost constant over the temperatures we measured, or no clear trend with temperature. The offset constant ϵ_{∞} in equation (1) is decided by the level of continuum at the wavenumber higher than 1200 cm^{−1} where slight variations of that level were observed in our measurements as the sample temperature changed, but they were neither stable nor reproducible. We assumed the value ϵ_{∞} is constant for each axis considering the smallness of the variation, and adopted the optimal values derived in Sogawa et al. (2006).

4 ABSORPTION SPECTRA

Calculating the absorption spectra with our oscillator parameters, we are able to predict the spectra of crystalline forsterite particles in astronomical observations. Absorption spectra depend on the shape and size distribution of particles, and the readily computable cases of Rayleigh approximation of spherical and continuous distribution of ellipsoids (CDE) are considered here as representative examples (Bohren & Huffman 1983). Spherical shape assumption under Rayleigh approximation predicts the absorption features to be very sharp and strong providing an extreme case. The CDE model often

Table 1. Forsterite oscillator parameters for temperatures from 295 to 50 K. ω_j is in cm^{-1} and S_j/ω_j^2 , γ_j/ω_j are non-dimensional.

	Axis a (B_{3u}) $\epsilon_\infty = 2.77$			Axis b (B_{2u}) $\epsilon_\infty = 2.66$			Axis c (B_{1u}) $\epsilon_\infty = 2.71$		
	ω_j	S_j/ω_j^2	γ_j/ω_j	ω_j	S_j/ω_j^2	γ_j/ω_j	ω_j	S_j/ω_j^2	γ_j/ω_j
T 295 K	976.4	3.28e-01	6.88e-03	984.2	7.23e-03	5.14e-03	874.1	6.13e-01	6.16e-03
	958.0	1.62e-01	3.81e-03	871.8	3.84e-01	3.20e-03	502.9	4.34e-01	1.97e-02
	840.9	4.03e-03	1.00e-02	837.8	1.29e-01	1.13e-02	476.2	1.52e-01	1.69e-02
	604.0	2.19e-01	2.09e-02	526.9	1.77e-01	2.37e-02	415.1	9.37e-01	1.36e-02
	501.7	3.48e-01	2.56e-02	506.0	4.37e-02	1.25e-02	408.4	4.87e-01	1.38e-02
	402.3	1.53e+00	1.39e-02	455.9	1.87e-01	1.95e-02	304.5	2.89e-02	1.52e-02
	379.2	9.80e-01	1.45e-02	416.8	2.77e-01	1.30e-02	291.1	1.23e+00	1.01e-02
	319.6	8.31e-02	8.71e-03	395.1	4.62e-01	1.35e-02	276.1	8.03e-02	9.51e-03
	294.2	3.24e-01	1.17e-02	348.7	1.21e+00	1.57e-02			
	274.8	5.27e-02	9.80e-03	289.1	1.63e+00	1.53e-02			
	200.9	2.55e-02	1.22e-02	276.8	8.37e-02	9.13e-03			
				143.4	7.80e-02	1.45e-02			
T 200 k	977.4	3.26e-01	5.71e-03	985.5	7.19e-03	4.39e-03	874.7	6.12e-01	5.87e-03
	959.1	1.69e-01	3.21e-03	872.9	3.93e-01	3.10e-03	504.4	4.31e-01	1.58e-02
	841.0	4.57e-03	9.14e-03	838.2	1.16e-01	9.03e-03	477.4	1.66e-01	1.25e-02
	605.4	2.25e-01	1.65e-02	528.0	1.65e-01	1.86e-02	417.3	8.77e-01	1.02e-02
	502.8	3.31e-01	1.71e-02	506.9	4.90e-02	9.68e-03	410.5	5.40e-01	8.83e-03
	403.6	1.45e+00	8.30e-03	457.2	1.90e-01	1.50e-02	305.6	3.20e-02	9.34e-03
	381.2	1.00e+00	9.73e-03	418.6	2.57e-01	9.36e-03	292.2	1.22e+00	6.92e-03
	320.4	8.49e-02	5.31e-03	396.4	4.88e-01	1.03e-02	277.4	8.90e-02	6.23e-03
	295.2	3.23e-01	7.69e-03	350.5	1.22e+00	1.06e-02			
	275.9	4.98e-02	6.31e-03	290.2	1.63e+00	9.40e-03			
	201.9	2.97e-02	7.81e-03	277.9	7.11e-02	5.64e-03			
				144.2	7.78e-02	8.96e-03			
T 150 K	977.7	3.25e-01	5.08e-03	986.1	7.17e-03	4.08e-03	874.7	6.13e-01	5.46e-03
	959.5	1.69e-01	2.78e-03	873.0	3.96e-01	2.89e-03	505.2	4.38e-01	1.37e-02
	841.7	6.34e-03	9.10e-03	838.6	1.13e-01	8.24e-03	478.3	1.71e-01	9.94e-03
	605.6	2.19e-01	1.40e-02	528.2	1.63e-01	1.66e-02	418.1	8.61e-01	8.92e-03
	503.6	3.38e-01	1.59e-02	507.4	5.14e-02	8.22e-03	411.1	5.55e-01	6.63e-03
	404.4	1.48e+00	7.75e-03	457.7	1.92e-01	1.27e-02	306.0	3.45e-02	5.80e-03
	382.0	9.94e-01	7.54e-03	419.3	2.50e-01	7.45e-03	292.5	1.20e+00	4.49e-03
	320.6	8.91e-02	4.26e-03	396.9	5.01e-01	9.09e-03	277.9	8.06e-02	3.60e-03
	295.3	3.32e-01	6.12e-03	351.4	1.22e+00	7.93e-03			
	276.2	4.60e-02	3.97e-03	290.8	1.62e+00	6.84e-03			
	202.4	2.82e-02	4.44e-03	278.2	5.64e-02	3.84e-03			
				144.5	6.81e-02	5.30e-03			
T 100 K	978.0	3.23e-01	4.70e-03	986.4	7.13e-03	3.90e-03	874.6	6.13e-01	5.15e-03
	959.7	1.73e-01	2.73e-03	873.1	3.96e-01	3.07e-03	505.3	4.30e-01	1.25e-02
	841.6	4.87e-03	8.18e-03	838.7	1.11e-01	7.78e-03	478.4	1.78e-01	8.71e-03
	605.9	2.30e-01	1.31e-02	528.6	1.62e-01	1.48e-02	418.6	8.16e-01	7.62e-03
	504.5	3.46e-01	1.19e-02	507.7	5.37e-02	7.12e-03	411.5	6.26e-01	5.17e-03
	405.1	1.48e+00	6.32e-03	458.0	1.91e-01	1.09e-02	306.2	3.28e-02	2.69e-03
	382.9	9.53e-01	5.27e-03	419.8	2.42e-01	5.95e-03	292.8	1.20e+00	2.36e-03
	320.9	8.76e-02	2.93e-03	397.0	5.11e-01	7.66e-03	278.2	8.70e-02	2.34e-03
	295.8	3.25e-01	4.26e-03	351.8	1.24e+00	6.40e-03			
	276.5	4.39e-02	2.79e-03	290.8	1.63e+00	3.42e-03			
	202.5	2.42e-02	2.33e-03	278.6	6.19e-02	3.13e-03			
				144.7	6.79e-02	2.38e-03			
T 50 K	978.2	3.24e-01	4.47e-03	986.5	7.10e-03	3.84e-03	874.3	6.15e-01	4.29e-03
	959.9	1.71e-01	2.71e-03	873.2	3.97e-01	3.00e-03	505.5	4.34e-01	1.23e-02
	841.3	5.51e-03	7.84e-03	838.7	1.11e-01	7.61e-03	478.7	1.76e-01	7.72e-03
	606.1	2.27e-01	1.24e-02	528.8	1.55e-01	1.38e-02	418.8	8.09e-01	6.67e-03
	504.8	3.54e-01	1.21e-02	507.6	5.36e-02	6.56e-03	411.6	6.26e-01	4.23e-03
	405.2	1.49e+00	4.90e-03	458.0	1.91e-01	1.05e-02	306.3	3.19e-02	1.27e-03
	383.2	9.58e-01	3.97e-03	419.9	2.42e-01	4.99e-03	292.7	1.21e+00	1.44e-03
	321.1	8.40e-02	2.03e-03	397.1	5.20e-01	6.26e-03	278.3	8.95e-02	1.78e-03
	296.0	3.18e-01	3.19e-03	352.0	1.22e+00	3.44e-03			
	276.7	4.83e-02	2.49e-03	290.9	1.61e+00	1.99e-03			
	202.6	2.30e-02	1.26e-03	278.7	8.15e-02	3.07e-03			
				144.8	6.97e-02	8.77e-04			

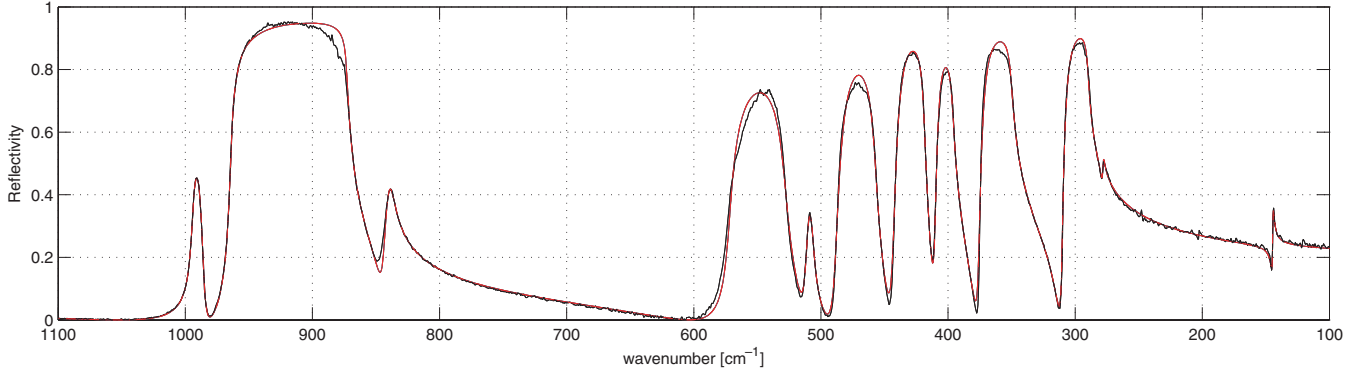


Figure 5. Comparison of the measured and calculated spectra for axis b , $T = 200$ K as an example. Black line is for the measured data and red line is for the calculation using the derived oscillator parameters.

provides reasonable agreement to the absorption measurements of powder in laboratories (Sogawa et al. 2006). For these shape distributions, the absorption cross-sections per unit mass by small particles in vacuum are calculated as

$$\kappa_{\text{SPHERE}} = \frac{2\pi}{\lambda\rho} \text{Imag} \left(\frac{\epsilon - 1}{\epsilon + 2} \right) \quad (3)$$

and

$$\kappa_{\text{CDE}} = \frac{2\pi}{\lambda\rho} \text{Imag} \left(\frac{2\epsilon}{\epsilon - 1} \log \epsilon \right), \quad (4)$$

where ρ is the density of forsterite (3.27 g cm^{-3}), λ is wavelength and ϵ is the dielectric constant given by equation (1). The above equations are for the case of isotropic dielectric constant ϵ , but ϵ for forsterite is anisotropic. As we do not know the exact way of calculation for anisotropic case, we adopt the conventional approximation and the average of cross-sections with equal weight, i.e.

$$\frac{[\kappa(\epsilon_a) + \kappa(\epsilon_b) + \kappa(\epsilon_c)]}{3} \quad (5)$$

is used as the final cross-section of forsterite where ϵ_a , ϵ_b and ϵ_c are the dielectric constants for axis a , b and c , respectively.

Fig. 6 shows the absorption cross-section per unit mass in CDE case for temperature 295 and 50 K where the thermal alternation of the absorption features are observed, and larger variation are

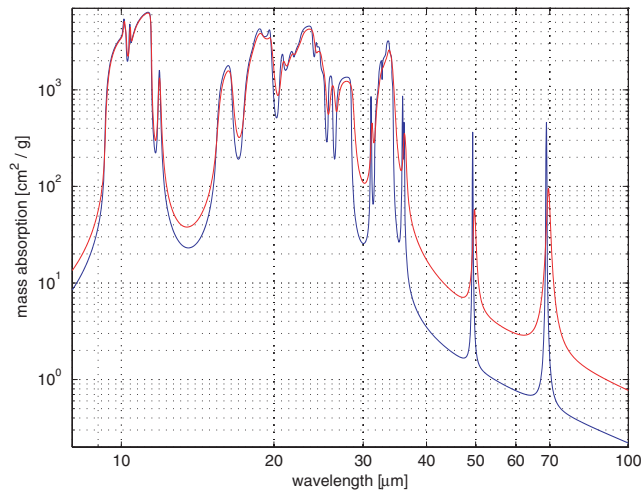


Figure 6. Absorption spectra of forsterite with the shape distribution of CDE. The absorption is in $\text{cm}^2 \text{ g}^{-1}$ and in log scale. Red line is for 295 K and blue for 50 K.

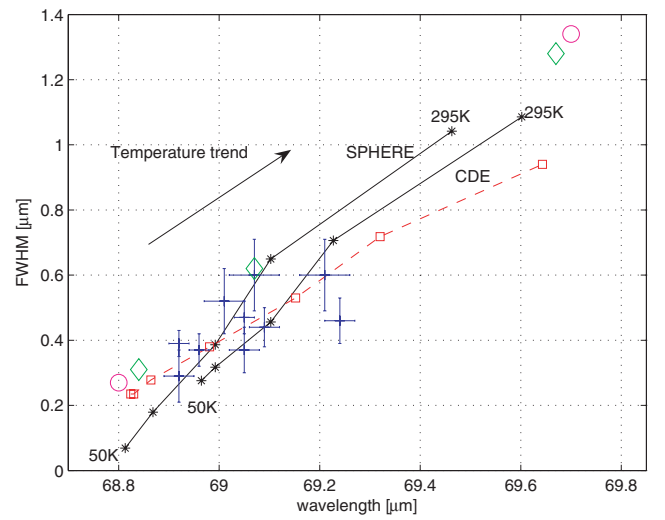


Figure 7. The relation of peak wavelength and FWHM along change of temperature for 69- μm feature. Asterisk marks are the points derived from the calculations for the particle shape of CDE and SPHERE at temperature 295, 200, 150, 100 and 50 K. The cross marks are observed points by ISO from Bowey et al. (2002). The diamond, circle and square marks are from laboratory particle absorption measurements of Bowey et al. (2002) ($T = 295, 77$ and 3.5 K), Chihara et al. (2001) ($T = 295, 4.2$ K) and Koike et al. (2006) ($T = 295, 200, 150, 100, 50, 20$ and 8 K).

seen at longer wavelength. The two isolated absorption peaks at 69 and 49 μm show drastic change of their intensities and widths with decreasing temperature. Multiplied with the blackbody radiation spectrum to the absorption spectra, the peak wavelength and FWHM of the features are derived for each temperature. The relation between FWHM and peak position for the 69- μm feature is shown in Fig. 7 along with temperature for the two cases of the shape distributions (CDE and spherical shape), where the relation is almost linearly stretched from 295 down to 50 K. The cross marks plotted in the figure (cross bar length stands for error value) are the observed points by ISO for the evolved and young dusty objects (Bowey et al. 2002). The observed points are aligned near the line of spherical or CDE case, but do not sit exactly on the lines. The scattering of the observed points across the calculated lines could be reflections of the shape variety of the cosmic forsterite, or it may be caused by the errors of measurements due to low spectral resolution of ISO observation, which was $0.29 \mu\text{m}$, too low to measure peak wavelength and FWHM of this feature as precise as in less

Table 2. Forsterite temperature estimation from peak wavelength of 69- μm feature. T_{Bowey} is from Bowey et al. (2002). T_{Koike} is based on the absorption measurements by Koike et al. (2006), T_{CDE} and T_{SPHERE} are the results of this paper for the particle shape distributions of CDE and SPHERE. The first column is object names, the second column is the observed peak wavelength of 69- μm feature (Bowey et al. 2002). For NGC 6537 and IRAS 16342, as their values of ($\lambda_{\text{peak}} + \text{error}$) are less than λ_{peak} at 50 K in CDE case ($\lambda_{\text{peak}}^{\text{CDE,50K}}$), upper limit of 50 K is applied. For NGC 6302, the λ_{peak} is less than $\lambda_{\text{peak}}^{\text{CDE,50K}}$, but ($\lambda_{\text{peak}} + \text{error}$) reaches on the CDE line at 78 K which is adopted as the upper limit.

Object	λ_{peak} (μm)	T_{Bowey} (K)	T_{Koike} (K)	T_{CDE} (K)	T_{SPHERE} (K)
NGC 6537	68.92 ± 0.02	28 ± 6	74 ± 9	<50	121 ± 8
IRAS 16342	68.92 ± 0.03	27 ± 10	74 ± 13	<50	121 ± 12
NGC 6302	68.96 ± 0.02	41 ± 6	91 ± 9	<78	137 ± 8
OH 26.5+0.6	69.01 ± 0.04	57 ± 14	108^{+12}_{-13}	108^{+18}_{-48}	158^{+18}_{-17}
CPD -56°8032	69.05 ± 0.02	70 ± 7	120 ± 6	126 ± 9	176 ± 9
AFGL 5379	69.05 ± 0.03	69 ± 8	120 ± 9	126 ± 14	176 ± 14
HD 44179	69.07 ± 0.05	77 ± 16	126 ± 15	135^{+22}_{-23}	185^{+19}_{-23}
HD 101584	69.09 ± 0.03	84 ± 9	132 ± 9	144^{+13}_{-14}	194^{+10}_{-14}
HD 100546	69.21 ± 0.05	127 ± 18	167 ± 15	193^{+15}_{-20}	228 ± 13
MWC 922	69.24 ± 0.03	139 ± 10	176 ± 9	203^{+8}_{-10}	236 ± 8

than 0.1 μm [eight of 10 observed points have the errors reaching on the line of CDE or spherical (SPHERE) case]. Laboratory data of particle absorptions (Chihara et al. 2001; Bowey et al. 2002; Koike et al. 2006) are also plotted in Fig. 7 where observed points are well aligned around the Koike’s measurements, which have the FWHM values lower than the other two absorption measurements. The temperature of forsterite for the observed objects are estimated with our calculations (CDE, SPHERE) and Koike’s measurements, and are listed in Table 2 along with the estimation by Bowey et al. (2002). As the errors of observed peak wavelength of 69- μm feature are less than errors of FWHM values, we relied on the observed peak wavelengths and compared them with laboratory results that are interpolated assuming the linear dependence of peak wavelength on temperature between the successive laboratory data points. The temperatures from our calculations (T_{CDE} , T_{SPHERE}) and Koike measurements (T_{Koike}) are 50–100 K higher than that of Bowey et al. (2002) (T_{Bowey}), where T_{SPHERE} shows highest temperature and T_{CDE} and T_{Koike} are comparable for the five of eight post-main-sequence objects. Since the dust temperatures estimated from the continuum slope (57–83 μm) for these objects are similar to those of T_{Bowey} , forsterite temperature can be much higher than those of dust responsible for the continuum emission. If one of T_{SPHERE} , T_{CDE} and T_{Koike} is adopted, crystalline dust should be localized in photon-enriched environments such as inner region or the surface of the circumstellar discs while amorphous dust distributes over extended cooler regions.

There are discrepancies between the results of FWHM and peak wavelengths obtained by the absorption and reflection measurements. The difference of FWHM values of these two laboratory works may be due to the spectral resolution which is not enough for sharp features at low temperatures, and due to the difference of continuum level underlying the feature at higher temperature. The continuum levels seen in absorption measurements are one order or more higher than the predictions from oscillator parameters, which would be the scattering caused by aggregated particles, and that hampers correct estimation of feature shape and intensity when the feature intensity is weak compared to continuum level at higher temperature. The difference of peak wavelengths could be due to adoption of simple shape distribution of particles such as SPHERE and CDE which may not approximate well the real shape distribution of particles in the absorption measurements. More sophisti-

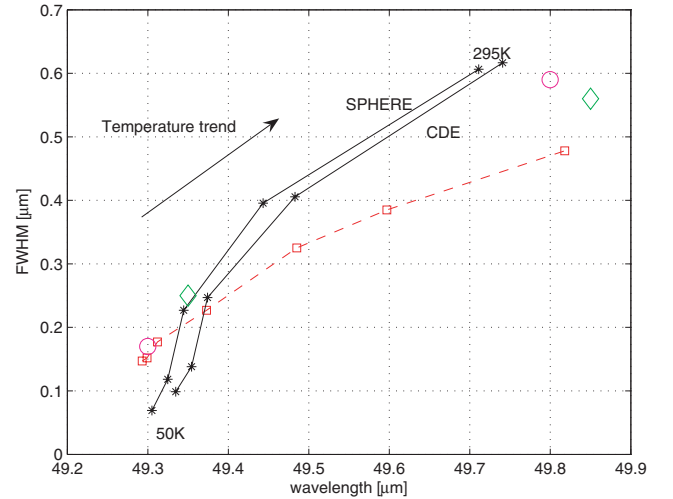


Figure 8. The relation of peak wavelength and FWHM along change of temperature for 49- μm feature. The marks are the same as in Fig. 7.

cated model taking real particle shape into account could relieve the difference, but so far we have no clear explanation.

For the 49- μm feature, as shown in Fig. 8, a large change of peak wavelength is observed down to 100 K, and the temperature evolution of FWHM is seen down to 50 K although it becomes less. This feature is another good temperature indicator in low-temperature environments (Koike et al. 2006). Although the detection of this feature by *ISO* was difficult owing to the steep-rising continuum and the higher noise level at 49- μm region (Bowey et al. 2002), further reductions of *ISO* data and analysis comparing with laboratory measurements are desired to improve temperature estimation of crystalline dust combining with 69- μm feature. The deviations of our predication from absorption measurements are seen which are similar to the 69- μm feature. We should search for the reasons of these disagreements to establish robust estimation scheme of temperature.

Although these two features at 69 and 49 μm show distinct evolutions with temperature, the absolute shift of peak wavelength and the change of FWHM are of the order of 0.1 μm between 100 and 50 K, therefore wavelength resolution higher than 1000 is requested

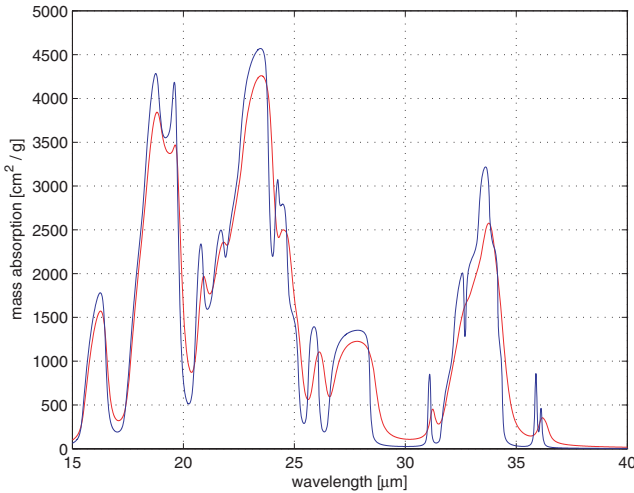


Figure 9. Absorption spectra of forsterite between 15 and 40 μm with shape distribution of CDE. The absorption is in $\text{cm}^2 \text{g}^{-1}$ and in linear scale. Red line is for 295 K and blue for 50 K.

for the future infrared observations so that the more reliable estimation of temperature and shape of forsterite crystal would be possible with more elaborated dust model.

For the shorter wavelength region, there are notable features at 16, 19, 23, 26, 28, 31, 33 and 36 μm as shown in the case of CDE in Fig. 9. As temperature decreases, these features shift towards shorter wavelength with the development of the trough at 32.7 μm , and double peak at 36 μm , which were confirmed by laboratory absorption measurements of forsterite particles (Bowey et al. 2001; Koike et al. 2006). The relative intensities between the features can be used to estimate temperature and the precise observation of their peak positions and feature shape would bring finer evaluation of dust temperature. For Comet Hale-Bopp, four of the above features, 19, 23, 28 and 33 μm were clearly observed which were attributed to crystalline forsterite with little contributions from enstatite (Crovisier et al. 1997). The intensity ratios of the features 19, 23 and 33 μm are not consistent with any blackbody radiation while small intensity of 33- μm feature suggested that the dust temperature should be higher than the equilibrium temperature of 160 K at 2.9-au heliocentric distance (Brucato et al. 1999; Min et al. 2005). The observed 33- μm feature did not show a trough implying that the crystalline dust temperature is around or higher than 200 K, which is consistent with the analysis by Brucato et al. (1999). For the circumstellar regions of the evolved stars, prominent features at 19, 23, 33 and 43 μm were observed (Molster et al. 2002) where the features are considered to be sum of those from forsterite and enstatite. Strong features at 33 μm are observed for many of them suggesting that the dust temperature is as low as 100 K (Molster et al. 2002). As enstatite is also a major contributor for the crystalline features for these objects, the study of its optical behaviour at low temperature is important (Bowey et al. 2001), and its optical constant at low temperature is highly desired in reproducing the observed spectra correctly that enable accurate temperature evaluation of crystalline silicates.

The features around 10 μm are accessible from the ground-based telescopes and the crystalline silicates around YSOs and evolved stars are widely observed at this wavelength, and variations of its shape and wavelength shift are found (Honda et al. 2004; van Boekel et al. 2005). As the features of forsterite around 10 μm are stable against the temperature change below 295 K, the observed variations

of 9–11 μm crystalline features cannot be explained with the change of temperature of crystalline forsterite at cold environment, while the composition, shape, size and the degree of fractal of dust should be the main factor for the variations.

5 CONCLUSIONS

We measured the reflection spectra of crystalline forsterite for temperatures from 295 to 50 K and derived a set of oscillator parameters by fitting the reflection spectra with the damped oscillator model. Our oscillator parameters reproduce the reflection measurements fairly well and the optical constants derived from them provide an essential utility for the studies of optical characters of forsterite in low-temperature environments. The expected absorption spectra by forsterite powder were calculated in Rayleigh approximation for spherical shape and CDE case, and the temperature dependence of the features was presented where the isolated features at 69 and 49 μm are promising temperature gauge for cool forsterite dust.

ACKNOWLEDGMENTS

We thank Prof H. Okuda for his continuous support of our cosmic dust research. We were supported by Grants-in-Aid from the Japanese Ministry of Education, Culture, Sports, Science, and Technology (12440054, 15340064) as well as National Astronomical Observatory of Japan.

REFERENCES

- Bohren C. F., Huffman D., 1983, *Absorption and Scattering of Light by Small Particles*. Wiley-Interscience Publication, New York, p. 356
- Bowey J. E., Lee C., Tucker C., Hofmeister A. M., Ade P. A. R., Barlow M. J., 2001, *MNRAS*, 325, 886
- Bowey J. E. et al., 2002, *MNRAS*, 331, L1
- Brucato J. R., Colangeli L., Mennella V., Palumbo P., Bussoletti E., 1999, *Planet. Space Sci.*, 47, 773
- Chihara H., Koike C., Tsuchiyama A., 2001, *Publ. Astron. Soc. Jpn.*, 53, 243
- Crovisier J., Leech K., Bockelee-Morvan D., Brooke T. Y., Hanner M. S., Altieri B., Keller H. U., Lellouch E., 1997 *Sci*, 275, 1904
- Fabian D., Henning T., Jäger C., 2001, *A&A*, 378, 228
- Hofmeister A. M., 1987, *Phys. Chem. Miner.*, 14, 499
- Honda M., Katata H., Okamoto Y. K., Miyata T., Yamashita T., Sako S., Takubo S., Onaka T., 2003, *ApJ*, 585, L59
- Honda M. et al., 2004, *ApJ*, 610, L49
- Iishi K., 1978, *Am. Mineral.*, 63, 1198
- Koike C. et al., 2006, *A&A*, 449, 583
- Malfait K., Waelkens C., Waters L. B. F. M., Vandenbussche B., Huygen E., de Graauw M. S., 1998, *A&A*, 332, L25
- Maradudin A. A., Wallis R. F., 1960, *Phys. Rev.*, 120, 442
- Min M., Hovenier J. W., de Koter A., Waters L. B. F. M., Dominik C., 2005, *Icarus*, 179, 158
- Molster F. J. et al., 1999, *A&A*, 350, 163
- Molster F. J., Waters L. B. F. M., Tielens A. G. G. M., Koike C., Chihara H., 2002, *A&A*, 382, 242
- Reynard B., 1991, *Phys. Chem. Miner.*, 18, 19
- Servoin J. L., Piriou B., 1973, *Phys. Stat. Sol. (b)*, 55, 277
- Sogawa H., Koike C., Chihara H., Suto H., Tachibana S., Tsuchiyama A., Kozasa T., 2006, *A&A*, 451, 357
- Takei F., 1978, *J. Cryst. Growth*, 43, 463
- van Boekel R., Min M., Waters L. B. F. M., de Koter A., Dominik C., van den Ancker M. E., Bouwman J., 2005, *A&A*, 437, 189
- Waelkens C. et al., 1996, *A&A*, 315, L245
- Waters L. B. F. M. et al., 1996, *A&A*, 315, L361
- Waters L. B. F. M. et al., 1998, *A&A*, 331, L61

This paper has been typeset from a \LaTeX file prepared by the author.